CRYSTAL
GROWTH
& DESIGN

Codesigning Tubular Flow and Noncontact Sonication for Antisolvent Crystallization: Rapid Fouling-Free Production of Uniform Rifapentine Crystals with Reduced Aspect Ratios

Sunuk Kim, Huayu Li, Richard D. Braatz, Tai-Yuen Yue, B. Frank Gupton, Bing-Shiou Yang, and Mo Jiang*

Cite This: https://doi.org/10.1021/acs.cgd.5c01079 Read Online

ACCESS | Metrics & More | Article Recommendations | Supporting Information

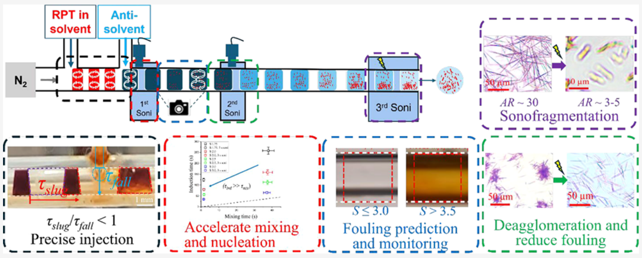

ABSTRACT: Rifapentine (RPT), a critical antituberculosis active pharmaceutical ingredient (API), faces persistent supply shortages compounded by crystallization challenges. Conventional antisolvent crystallization often produces RPT crystals with high aspect ratios (>7) and sizes outside the preferred 5−20 μm range. RPT's strong adhesion to solid surfaces further increases fouling risk, and makes conventional milling impractical due to equipment damage. To avoid fouling, prior processes have relied on low supersaturation (≤1.5), resulting in long residence times of 4−6 hours. This study introduces a modular, continuous, fouling-free crystallization process that simultaneously addresses these limitations by codesigning precise antisolvent injection, controlled supersaturation, and dynamic noncontact ultrasonication within a tubular slug-flow platform. We establish design criteria enabling reproducible antisolvent (water) injection into flowing RPT solution slugs (in tetrahydrofuran) via continuous droplet formation and merging, minimizing needs for feedback control or complex operation. Guided by simplified semiempirical models and rapid droplet/slug tests, noncontact sonication is strategically applied at three stages—nucleation, growth, and breakage—to suppress fouling and enhance uniformity, without needing milling. Within 0.5 hour of residence time, these steps collectively reduce crystal dimensions while maintaining small variations (e.g., length from 81 μm to 6 μm, coefficient of variation or $CV_L \sim 0.20$; aspect ratio from 33 to 3.5, $CV_{AR} \sim 0.29$) and 100% form purity. This integrated approach offers a scalable pathway toward reliable RPT crystallization and supply resilience.

1. INTRODUCTION

Rifapentine (RPT) is a long-acting antibiotic against *Mycobacterium tuberculosis*.[1] Global demand for RPT reached \$300 million (87.2 t) in 2024, up from \$200 million in 2021, and is projected to grow to \$500 million by 2027.[2] But supply in 2024 met only \$150 million (43.2 tons), constrained by profit and productivity.[2−4] With chemical synthesis cost already reduced by 30%, one potential solution is to reduce cost and operation time of downstream processes such as crystallization.[4]

RPT crystallization are mainly carried out by adding antisolvent,[5,6] with multiple common and inter-related issues on crystal quality and process consistency and efficiency. (1) Needlelike crystal morphology. As observed for many molecules, needlelike morphology often leads to poor solid filterability,[7,8] powder flowability,[9] bulk density,[10,11] and ultimately low dosage consistency and process efficiency.[7,12] The solid forms and corresponding morphology of RPT include most often the thermodynamically stable nonsolvate form ("Form I" in literature, needlelike crystals with aspect ratio, $AR > 5.0$), and sometimes amorphous (spherical aggregates), or organic solvates (needlelike).[13−16] Large aspect ratios are typically reduced through wet or spray milling, but these methods prolong processing, increase yield loss, and demand significant expertise.[6,17−21] (2) Large size or morphology variability. Crystal variability also reduced product quality and process efficiency.[22] Even the same needlelike morphology can demonstrate large coefficients of variability (CV) in dimension or aspect ratio, e.g., $CV_L \sim 0.55$, $CV_W \sim 0.27$, and $CV_{AR} \sim 0.41$ for RPT crystals.[6] Such variability arises from simultaneous phenomena during crystallization—nucleation, growth, attrition, agglomeration—and their nonuniform spatial distribution.[23−26] Continuous crystallizers aim to reduce variability, yet antisolvent injection still depends on operator experience. Near the injection point, local antisolvent concentration is higher than farther away, creating super-

Received: July 24, 2025
Revised: February 5, 2026
Accepted: February 6, 2026

Table 1. Literature Review on RPT Antisolvent Crystallization Conditions and Outcome[a]

RPT conc (g/l)	S_i	Solvent	Reactor	Crystallization method and condition	τ_{res} (hr)	Postcrystallization treatment	Crystal shape	Mean length (μm)	Mean aspect ratio	Recovery (%)	Ref
36	1.4	Acetone	Plug flow	Antisolvent (DI water), $w_{AS} = 0.5$, 50 °C, sonication	4	Spray drying milling	Needle and rod	1.9 ± 1.2	3.7 ± 2.1	30	6
36	3.5	Acetone	Plug flow	Antisolvent (DI water) $w_{AS} = 0.375$, 50 °C, sonication	1	Spray drying milling	Needle and rod*	2.9 ± 1.3	3.6 ± 1.6	43	6
36	3.0	Acetone	Plug flow	Antisolvent (DI water) $w_{AS} = 0.56$, 50 °C, sonication	2	Spray drying milling	Needle and rod*	3.3 ± 1.6	4.0 ± 1.3	48	6
23.8	1.2	Acetone	Batch	Antisolvent (DI water) $w_{AS} = 0.4$, Seeding	6	N/A	Needle *	15.2 ± 7.4	5.0 ± 2.3	2	5
25.2	1.3	Acetone	Batch	Antisolvent (DI water) $w_{AS} = 0.56$, Seeding	6	N/A	Needle *	16.3 ± 8.9	5.4 ± 2.0	19.2	5
28.2	1.4	Acetone	Batch	Antisolvent (DI water) $w_{AS} = 0.56$, Seeding	6	N/A	Needle *	3.5 ± 0.9	3.0 ± 1.3	21.6	5
4	1.0	Acetone/DI water	Batch	Evaporation at 67 °C	N/A	Spray drying milling	Needle and rod	1−10	6.0 ± 2.1	N/A	15
4	N/A	Methanol	Batch	Evaporation, with Nitrogen gas	N/A	Spray drying milling	N/A*	0.1−2	N/A	N/A	15
16	N/A	Acetone	batch	Evaporation at 67 °C	N/A	Spray drying milling	Needle and rod	0.9−3.3	2.9 ± 1.8	N/A	37
36.2	3.0	THF	Slug flow	Antisolvent (DI water) 20 °C, $w_{AS} = 0.5$, sonication	0.25	Sonication <0.2 h in same slug flow	Rod	6.1 ± 1.2	3.43 ± 1.0	63	This study

[a] S_i: initial supersaturation. τres: Residence time for nucleation and growth. w_{AS}: Antisolvent mass fraction. *: Mixture of crystals and amorphous solids. The term recovery (%) here refers to the mass ratio, between actual dried mass of crystal solid (after filtration and drying), and actual mass of total RPT at beginning. Another common term of yield was not used here to avoid repetition or confusion, which refers also to the mass ratio, but between the same denominator (actual dried mass of crystal solid) and different numerator (theoretical mass of RPT crystals from complete crystallization based on solubility).

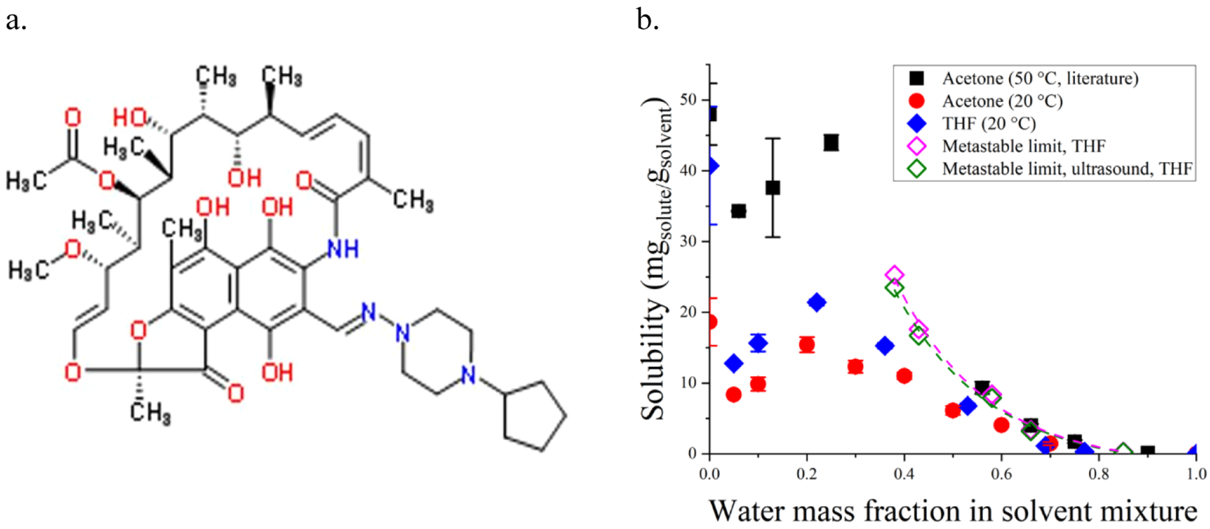

Figure 1. (a) Bond-line structure of RPT, (b) Solubility of RPT at room temperature in different solvents (acetone, ethanol, and THF), and at different mass fractions of the same antisolvent (water). Metastable limits (dashed line) in THF solvent with and without sonication are shown in olive and magenta, respectively.

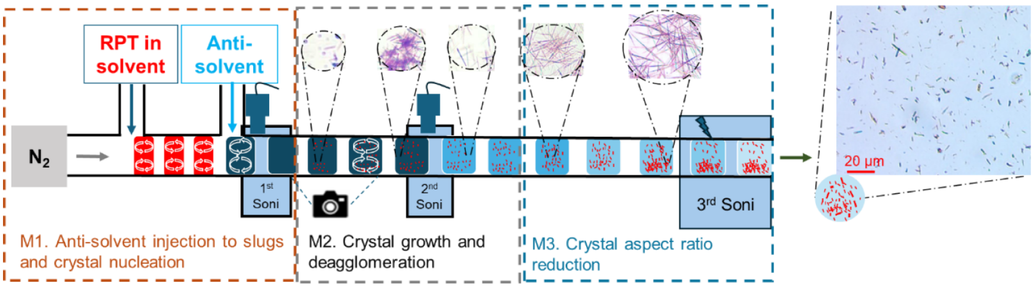

Figure 2. Schematic of process codesign for RPT antisolvent crystallization in slug flow with 3 sonication modules. Module M1: Formation of uniform slugs containing RPT solution and antisolvent, with sonication-aided nucleation; M2: Sonication-aided deagglomeration during crystal growth; and M3: Aspect ratio reduction for needle-shape crystals in ultrasonic bath.

saturation “hot spots” for secondary nucleation. Moreover, rapid solution flow requires subsecond feedback control, making precise injection challenging.

(3) Fouling. Fouling reduces yield, productivity, quality consistency, and operation supersaturation for batch or continuous crystallizations.[27−29] Wall fouling can result from multiple factors, including fast precipitation from high local supersaturation,[30] increased molecule-wall contact time from insufficient agitation and/or undesired morphology (e.g., needlelike),[31,32] or from high molecular stickiness,[33,34] etc. Sonication bath has been explored to increase agitation and improve supersaturation uniformity, with limited success on fouling mitigation.[35,36] (4) Long residence time. Extended time increases recovery, but reduces productivity, and increases the chances of fouling or thermal degradation. As in Table 1,[5,6,13,15,16,37] RPT crystallization from common initial supersaturation (S = 1.2−1.4) to avoid fouling or amorphous solids often needs 4−6 h to achieve reasonable recovery (e.g., 28%).[5,6] Increasing crystallization temperatures (e.g., 50 °C) to increase kinetics and solubility risk molecular thermal degradation. Such intertwined issue of fouling-recovery for RPT was insufficiently addressed.

This study aims to intensify the antisolvent crystallization process to address multiple challenges—large aspect ratio, size variability, fouling, and long residence time. RPT molecules that would otherwise foul surfaces or crystallize uncontrollably are redirected toward synchronized, accelerated nucleation, followed by controlled growth and aspect ratio reduction to yield uniform crystals. Specifically: (1) We derive design criteria to realize continuous, precise antisolvent injection into uniform solution slugs without needing feedback control or complex operation. (2) We codesign antisolvent crystallization with noncontact sonication in these slugs to ensure nonfouling nucleation and growth, producing uniform crystals (pure form, minimal degradation), even for large aspect ratios. (3) We extend this codesign to break down elongated crystals into uniform crystals with acceptable aspect ratios (3−7), guided by a simplified prediction model and optimized sonication time from rapid droplet/slug testing.

2. MATERIAL AND EXPERIMENTAL METHODS

2.1. Solvent Selection and Solubility Measurement

Rifapentine (RPT, MW 877 g/mol, 97%) was purchased from AA Blocks LLC and identified as Form I by XRD. The molecular structure of RPT is shown in Figure 1a. Acetone (Certified ACS) was obtained from Fisher Chemical, while ethyl alcohol (EtOH, 99.5%, ACS reagent) and tetrahydrofuran (THF, >99.9%, anhydrous) were purchased from Sigma-Aldrich. Commercial RPT was used as a reference standard for crystal characterization by XRD, DSC, TGA, and particle size distribution (Figure S1).

Tetrahydrofuran (THF) was chosen as the solvent for crystallization, for two reasons: (1) it was used in upstream synthesis, minimizing solvent exchange; and (2) despite its higher price ($7.6/L

Table 2. RPT Antisolvent Crystallization Conditions at Different Initial Supersaturations S_i, Crystallization Residence Time τ_{res}, or Postcrystallization Sonofragmentation Time t_s. w_{as} = 0.5 for All Crystallizers (SF for Slug Flow, B for Batch)

Experiment (# for S_i)	Initial conc (mg/g)	RPT solution volume (mL)	τ_{res} (min)	t_s (min)	L (μm)	CV_L	W (μm)	CV_W	AR	CV_{AS}	Recovery (%)	Crystal image
SF 1.75	23.8	0.16	60	0	39.1 ± 2.5	0.06	3.3 ± 1.1	0.33	14.2 ± 4.0	0.28	1.7	Figure S3a
SF 2.0	27.2	0.16	60	0	50.5 ± 8.0	0.15	3.1 ± 0.7	0.23	17.0 ± 4.3	0.25	8.3	Figure S3b
SF 2.5	34.0	0.16	60	0	61.4 ± 13.5	0.22	2.2 ± 0.5	0.23	28.4 ± 7.2	0.25	37.8	Figure S3c
SF 3.0	40.8	0.16	15	0	81.7 ± 10.4	0.13	2.4 ± 0.3	0.13	33.8 ± 5.6	0.17	62.9	Figure 6b, S3d
B 3.0	40.8	20	15	0	55.6 ± 21.4	0.38	2.7 ± 0.8	0.30	22.3 ± 11.0	0.49	61.5	Figure 6b
SF 3.0 SF	40.8	0.16	15	10	6.1 ± 1.2	0.20	1.9 ± 0.33	0.17	3.4 ± 1.0	0.29	63.0	Figure S4a
SF 3.0 _scale up	40.8	60	15	10	6.3 ± 1.5	0.23	1.84 ± 0.36	0.20	3.52 ± 0.9	0.26	61.6	Figure 8a

for THF vs \$4/L for acetone),[38,39] THF offers twice the solubility at pure solvent and more than twice the recovery at room temperature (e.g., concentration change 35 mg/g THF vs ∼15 mg/g acetone at 50% antisolvent mass fraction in Figure 1b), reducing solvent cost per unit crystal mass. Room-temperature was used for crystallization, as thermal degradation of RPT was observed at 50 °C (used in prior studies to increase solubility), e.g., HPLC-UV purity decreased from ∼97% to 80−90% after 1 h for both acetone and THF.

The solubility of RPT was evaluated in acetone and THF at room temperature using HPLC, across water mass fractions of 5−78 wt % for THF and 5−70 wt % for acetone. The metastable limit was determined visually by adding water dropwise to THF solutions at RPT concentrations of 3, 10, 20, 30, and 40.8 mg/g. For each solubility or metastable data point, 10 mL of solution was placed in a 50 mL round-bottom flask with an 8 mm magnetic stir bar, stirred at 500 rpm, and titrated with 50 μL water droplets at 60-s intervals.

2.2. Antisolvent Crystallization in Tubular Slug Flow

The slug-flow crystallizer (Figure 2) consisted of a solution feed channel, an antisolvent (deionized water) feed channel, a gas inlet, and three sonication units (two probes and one bath). Fluorinated ethylene propylene (FEP) tubing was selected for its compatibility with THF and its hydrophilic surface properties. An inner diameter of 3/32″ was chosen to ensure stable slug formation. RPT−THF solutions of various concentrations (Table 2) were prepared and filtered through a PVDF syringe filter prior to use. The RPT solution and DI water were delivered at 0.8 mL/min and 0.72 mL/min, respectively, using syringe pumps (New Era Pump Systems, Model NE-4000). Nitrogen gas (N_2) was introduced at 3 CCM via a mass flow controller (FMA-2617A, Omega). Residence times ranged from 15 to 60 min were controlled by adjusting the tubing length. Supersaturation profiles with initial S_i = 3.0 were established based on momentary solid recovery and RPT solution concentration measured or calculated at selected residence times (0.1−15 min) in Table S2. Transmitted-light intensity measurements used to determine τ_{mix}, τ_{ind}, and fouling behavior were extracted from video snapshots and analyzed using ImageJ.

2.3. Sonication Designs for Slug Flow

As in Figure 2, (1) the first sonication probe (VCX750, Sonics & Materials Inc., USA) was positioned 1 in. downstream of the T-junction for antisolvent injection to promote nucleation and mixing. (2) The second probe was placed near the tubular reactor point corresponding to the metastable limit to enable continuous deagglomeration of RPT needle-flower particles. Both probes operated at 20 kHz with 750 W input power and amplitudes of 80% and 100%, respectively; an 8.5 mm gap between probe and tubing preserved slug integrity during acoustic mixing. These probes enhanced slug mixing and nucleation, facilitating the formation of uniform particles with high aspect ratios. (3) The third ultrasonic bath (Branson CPX3800H, Bransonic Inc., USA) was installed at the reactor outlet to reduce crystal aspect ratios. It operated at 110 W and 40 kHz, corresponding to a sonication intensity of 0.9 W/cm^2. An exposure time of approximately 10 min for aspect ratio reduction was selected based on preliminary screening with a few slugs. The uniformity and reproducibility of slug flow ensure consistent crystal dimensions and time scales for larger-scale crystallization, even when scaling up by 4−6 orders of magnitude in slug number.[48,56−58] This sonication residence time can be adjusted without altering slug flow patterns by simply varying the length of tubing submerged in the sonication bath.[40,41] Crystal slurry slugs were collected at tubing exit, via vacuum filtration using 7 cm filter paper, washed with DI water, and dried at 50 °C under vacuum for 12 hours.

2.4. Crystal Characterization

Crystal morphology and variation were quantified using optical microscopy. Slurry samples were imaged with an optical microscope (NMM-800TRF, Amscope) equipped with a digital camera (DMK 37BUX250). Individual crystals were analyzed in ImageJ to determine their length and width, from which crystal-size statistics and aspect-ratio distributions (Tables S1−S3) were calculated. Crystalline forms were identified using powder X-ray diffraction (Rigaku MiniFlexII, Cu−Kα radiation, λ = 1.5406 Å), and normalizing diffractograms with the (0,1) method. These forms were then confirmed by differential scanning calorimetry (DSC Q1000, TA Instruments) with a heating rate of 10 °C/min from 40 to 200 °C. Solvate or hydrate states were evaluated using thermogravimetric analysis (TGA Q500, TA Instruments) from 20 to 200 °C at the same heating rate of 10 °C/min Figures 6 and 8.

3. RESULTS AND DISCUSSION

3.1. Develop Design Criteria for Continuous Precise Slug Injection of Antisolvent

The interval between adjacent slugs—only millimeters apart and moving at centimeters per second—is subsecond, imposing stringent requirements on in-line feedback control. Therefore, we focus on an intensified design to achieve precise control of solution composition, supported by in-line imaging. Rather than limiting injection to the brief exposure of slugs at the injection point, we also leverage interval time between adjacent slugs. Specifically, instead of targeting flowing slugs for continuous antisolvent injection, we generate discrete antisolvent droplets and merge each with its corresponding solution slug. This design satisfies three critical conditions for uniform size and stability: (1) Hydrodynamic stability of slugs before and after injection (e.g., total slug count remains unchanged); (2) Volumetric stability and reproducibility of injection droplets prior to merging; and (3) Precise timing of slug-droplet merging, ensuring the next slug reaches the

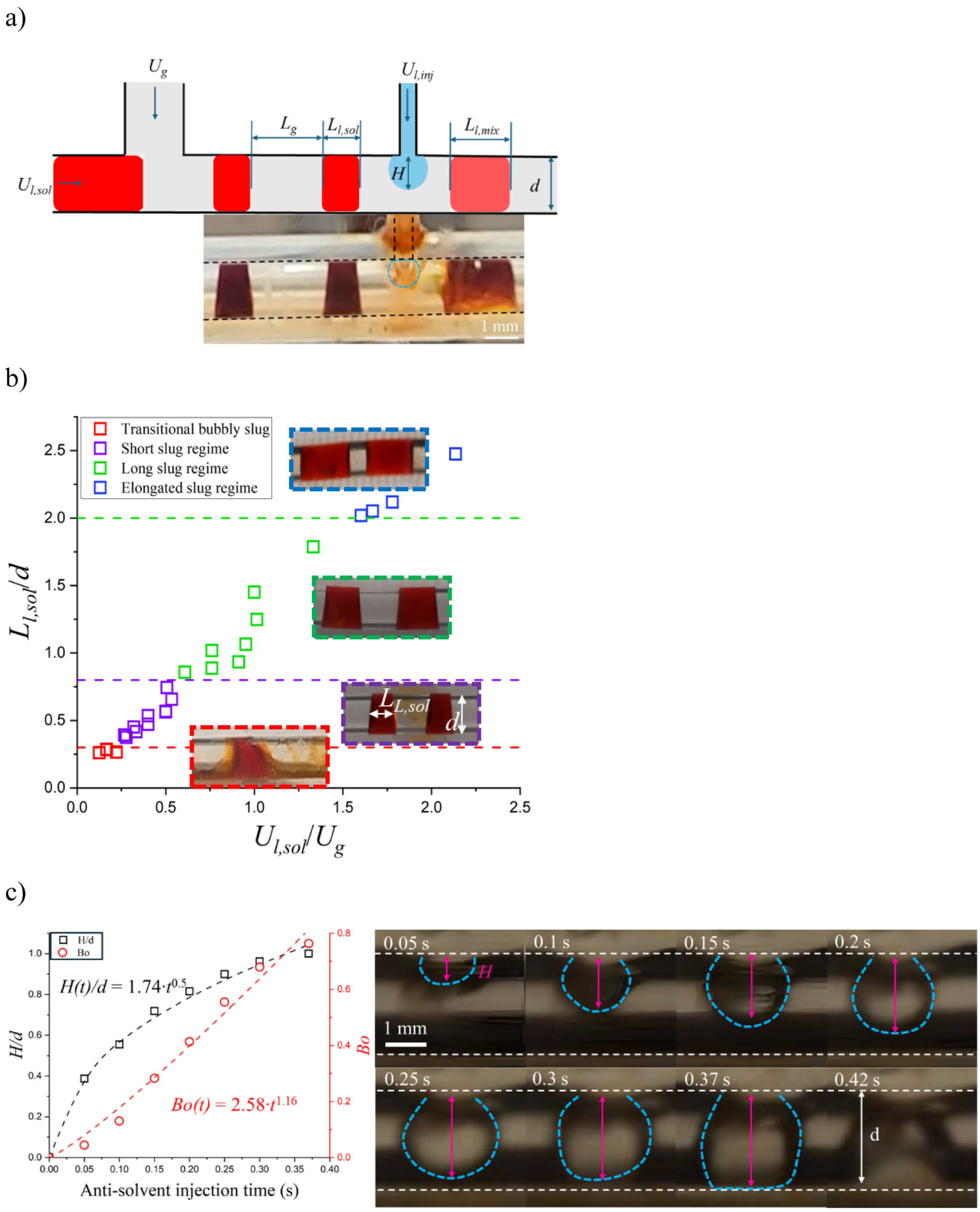

Figure 3. (a) Schematic and video snapshot of precise antisolvent injection to flowing slugs, with key variables labeled. (b) Length regimes of uniform-size stable slugs. (c) Change of antisolvent droplet height (H) and corresponding Bond number (Bo) over antisolvent injection time at an injection rate of 0.72 mL/min, based on in-line video snapshots.

injection point as the droplet reaches a defined volume, such as when contacting the tubing bottom.

1 Hydrodynamic stability of flowing slugs before and after injection. We categorize the stable slug-flow regime reported in literature[42−44] (gas and liquid flow rates), into practical subregimes of uniform slug lengths (e.g., Figure 3b), based on preliminary tests showing that slug length for a given tubing also depends on gas and liquid flow rates. Although these regimes were originally developed for gas−liquid systems without liquid injection, our experiments indicate that final slug length is primarily determined by the total liquid-to-gas mass ratio (Figure S2b), regardless of whether liquid originates solely from the solution ($L_{L,sol}$) or includes injected liquid ($L_{L,mix}$). For stability confirmation, we adopt the stable slug-flow regime for injection, defining U_L as the effective liquid velocity based on total liquid mass. While maintaining slug stability with the total liquid, the internal liquid ratio—such as the antisolvent mass fraction (w_{AS})—can be adjusted to meet super-

saturation or solubility requirements. For example, after specifying w_{AS} = 0.5 based on solubility (Figure 1b), solution slugs can be generated continuously within the "short slug regime" ($0.3 < L_{L,sol}/d < 0.6$ for tubing I.D. of 2.38 mm), ensuring stability even after injection-induced volume increase, or within the "long slug regime" (canonical Taylor regime, $0.8 < L_{L,mix}/d < 1.2$). In practice, slugs were produced by controlling gas and liquid flow rates via pumps or mass-flow controllers (e.g., Q_G = 1.5 − 3 mL/min, $Q_{L,sol}$ = 0.8 − 1.2 mL/min, and $Q_{L,inj}$ = 0.72 − 1.1 mL/min), corresponding to the "purple" and "green" regimes in Figure 3b for solution and solution−antisolvent mixture slugs, respectively.

2 Volumetric stability of droplet before merging. At a constant injection flow rate (fixed φ), the droplet at the injection inlet grows in diameter and height (H) until it either contacts the opposite tubing wall ($H \approx d$) or falls under gravity when surface tension can no longer counteract it (Bond number $Bo > 1$), whichever occurs first. This time is recorded as τ_{fall}. Quick but reproducible in-line video tests based on small number of droplets show that droplets grow until touching the opposite wall (Figure 3c), following an empirical correlation of $H(t) = A_h{\cdot}t^B$ for $0 \le t \le \tau_{fall}$, where A_h and B are fitting coefficients. For example, at a volumetric injection rate of 0.72 mL/min ($U_{L,inj}$ = 27 mm/s), $H(t) = 1.74{\cdot}t^{0.5}$, and $\tau_{fall} \approx 0.235$ s for $H = d$ = 2.4 mm ($Bo \approx 0.8$). τ_{fall} can be increased without changing equipment configuration by reducing the liquid injection rate. The power B = 0.5 also aligns with theoretical analysis in literature, indicating the droplet pinch-off was dominated by liquid inertia.[45]

3 Precise timing for droplet merging. The next solution slug (τ_{slug} after the prior one) shall reach the injection point before the antisolvent droplet contacts the opposite wall (τ_{fall} after the prior merging), satisfying $\tau_{slug}/\tau_{fall} < 1$. τ_{slug} comprises the time for a solution slug to traverse the gap between adjacent solution slugs ($\sim L_G$) and the injection zone ($L_{L,sol}$), at a velocity of ($U_{L,sol} + U_G$), thus $\tau_{slug} = (L_G + L_{L,sol})/(U_{L,sol} + U_G)$. The slug lengths were correlated to pumped gas and solution flow rates as in literature,[46,47] where $L_{L,sol} = d[1 + 0.08(U_{L,sol}/U_G)][U_{L,sol}/(U_{L,sol}+U_G)]$, and $L_G = 0.16d(U_{L,sol}/U_G)^{-1.39}$. Both τ_{slug} and τ_{fall} were confirmed with in-line imaging (Figure 3a,c). The injection precision is confirmed with small coefficients of variation CV_V, both in solution slug volume (0.014), and slug volume increase after injection (0.013). As in Figure S2a, slugs before injection have an average length of ~0.9 mm, and volume of 4.2 μL, and after injection a length of ~1.8 mm, and volume of 8.4 μL.

3.2. Codesign Sonication and Supersaturation for Nonfouling Uniform Nucleation and Growth

The precise injection strategy described above ensures that each slug experiences identical physicochemical conditions during crystallization. To achieve a nonfouling process that avoids needlelike morphology, we focus on the codesign of flow, supersaturation, and noncontact sonication within a representative slug. For proof-of-concept, supersaturation is increased once through a single antisolvent injection, making the peak (initial) supersaturation the primary design variable. Because fouling typically initiates near peak supersaturation during nucleation, this section focuses on preventing fouling at the nucleation stage. Process parameters were first screened in small-scale tests (0.16 mL, 4 slugs, to determine sufficient sonication time; and 2 mL, ~50 slugs, to evaluate fouling at peak-supersaturation locations) and then validated in larger-scale production (e.g., 60 mL).

Uniform nucleation without fouling: (1) Supersaturation design: Uniform nucleation requires spatially uniform supersaturation and the elimination of local supersaturation hotspots. This is achieved by ensuring that nucleation does not begin until mixing is complete (i.e., satisfying $\tau_{mix} \ll \tau_{ind}$).[48] Induction time decreases with increasing initial supersaturation, but higher supersaturation also increases fouling propensity. Conversely, higher supersaturation accelerates crystallization kinetics and improves recovery (Table 1), creating a design trade-off. The initial supersaturation is controlled by adjusting the antisolvent mass fraction. S_i = 3.0 was selected based on estimation from a simplified fouling model for crystallization at different slug flow rates[49,50] (Figure 4), that fouling is negligible for $S_i \le 3.0$ at 0.017 m/s and for $S_i \le 2.5$ at 0.011 m/s. (2) Sonication design: Sonication is applied immediately after antisolvent injection, when the risk of local supersaturation hotspots is highest. The hypothesis is that brief sonication reduces mixing time more significantly than induction time, thereby satisfying $\tau mix \ll \tau_{ind}$ and preventing premature nucleation at the slug wall. Preliminary tests at S_i = 2 support this hypothesis: sonication reduced mixing time by ~20-fold (37 s → 1.7 s) but reduced induction time by only ~2-fold (e.g., 150 s → 75 s), as in Figure 5a. This differential reduction enables controlled nucleation without fouling.

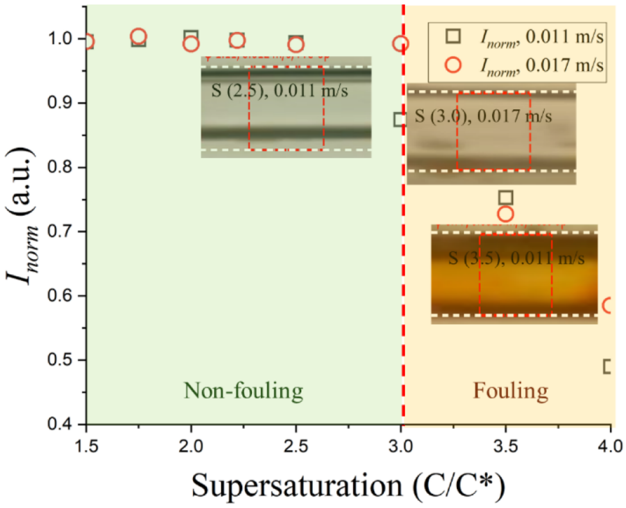

Figure 4. Fouling situation predicted by the supersaturation-based fouling rate model in Appendix A1, validated through visual inspection and normalized overall transmitted-light intensity from in-line video snapshots. Transmission intensity reduction indicates fouling. Two slug velocities (0.011 and 0.017 m/s) were evaluated. The fouling threshold (fouling rate F_r = 0) is indicated by the dotted line.

Figures 4 and 5 confirm the nonfouling performance and reproducible nucleation behavior. Fouling was observed ~5 s downstream of the antisolvent injection point for S_i = 3.5 (w_{AS} = 0.6), but not for $S_i \le 3.0$. At S_i = 3.0, τ_{ind} and τ_{mix} were 70 and 36 s, respectively. With sonication, mixing time decreased

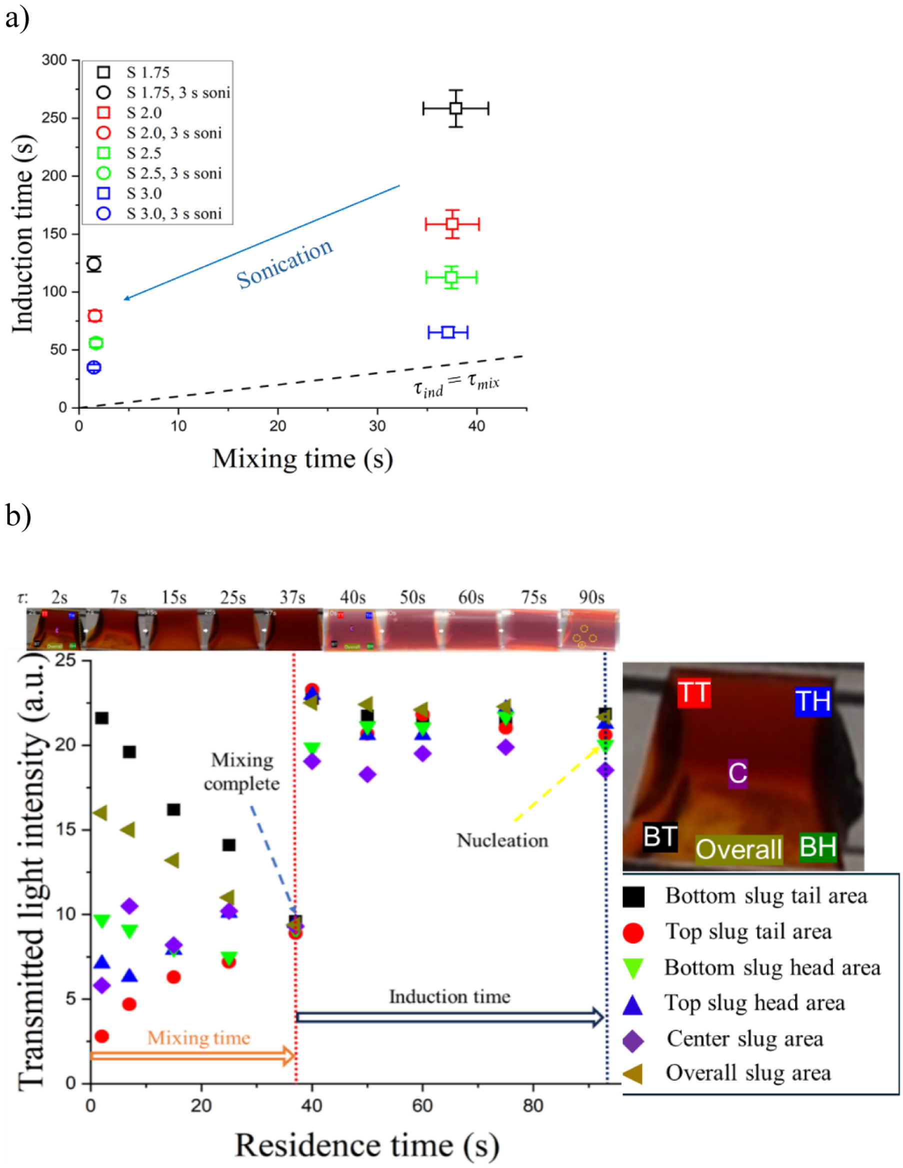

Figure 5. (a) Mixing and induction times in representative slugs, with error bars indicating standard deviations from triplicate measurements. (b) Example analysis corresponding to panel (a), based on visual inspection and changes in normalized transmitted-light intensity from in-line slug video snapshots. Measurements were taken at six locations within each slug (BT: bottom tail; TT: top tail; TH: top head; BH: bottom head; C: center; and overall, for the target slug). Mixing time is defined as the point at which intensities at different locations converge, while induction time corresponds to the first observable appearance of solids within the slug.[51] The background light intensity before and after 38 s (∼mixing time) was different.

by 18-fold while induction time decreased by 2.2-fold, realizing $\tau_{\text{mix}} < 0.1\tau_{ind}$. The resulting nuclei (Figure 6b) exhibited low size variation (CV = 0.1) with an average size of ∼3 μm. Achieving S_i = 3.0 at room temperature eliminates the need for elevated temperatures (e.g., 50 °C), reducing thermal degradation risk.

Uniform growth design: Preliminary tests (Figure 6a−b) show that needle-shaped crystals form across a wide supersaturation range (S_i = 1.75−3.0). At $S_i \geq 2.5$, agglomeration becomes significant, broadening the particle size distribution even in slug flow. This likely arises because growth and agglomeration occur simultaneously but with different kinetics and morphological pathways. Reducing S_i to 1.75−2.0 suppresses agglomeration (Figure S5), but at the cost of reduced recovery and productivity. Sonication can break agglomerates, but batch sonication fields are spatially nonuniform, leading to inconsistent breakage (Figure 6c). To achieve uniform growth, the slug flow tubing is placed within a sonication field (probe or bath), leveraging the inherent uniformity of slug volumes to generate effective, uniform, noncontact "milli-fields" within slugs.[40,41] Sonication is applied briefly (e.g., 3 s per slug), and shortly after agglomeration begins to form and when the concentration approaches the metastable limit. This timing prevents loose agglomerates from densifying into aggregates[52] that are more difficult to break and that broaden the size distribution (Figure 6b,c). In this work, agglomerate-breaking sonication was applied ∼5 min downstream of the first sonication, based on preliminary studies of agglomeration and supersaturation dynamics using 4−5 slugs.

With the flow−supersaturation−sonication codesign, crystals produced at S_i = 3.0 exhibit good uniformity (CV_L = 0.13, CV_W = 0.13, and CV_{AR} = 0.17) without fouling or

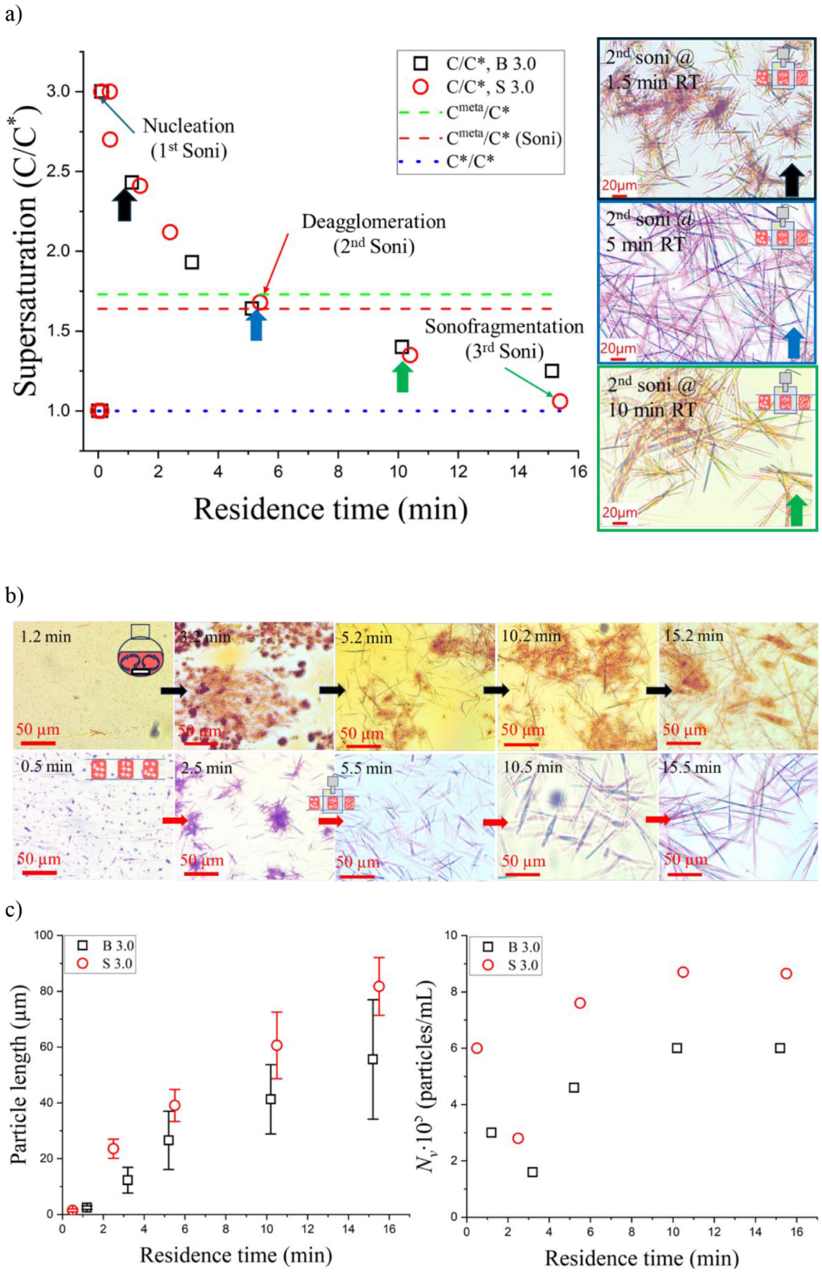

Figure 6. (a) Supersaturation time profiles and three sonications for representative slugs Microscopy images of deagglomeration product crystals (2nd sonication) are shown for residence time of 1.5, 5, and 10 min. (b) Microscopy images from representative slugs in (a) and batch crystallization at same initial supersaturation of 3.0. (c) Particle length and number density at different residence times for (b), with statistics in Table S2. For growth comparison, aggregates composed of multiple crystals are treated as one particle.

agglomeration, even at large sizes (average length ∼82 μm) and high aspect ratios (average ∼34). The residence time required to reach theoretical recovery is reduced to 0.25 h (Figure 7), compared to 4–6 h reported in the literature. The spatial uniformity of both peak supersaturation and sonication fields results in crystals with less agglomeration and narrower size distributions than those produced in batch under identical supersaturation conditions, despite faster kinetics and larger crystal sizes in slug flow (Figure 6c). Although batch crystallization produces more total crystals (Figure 6b), many are agglomerates counted as single particles with large surface area, reducing the apparent number density and slowing apparent growth rates. The high aspect ratios and uniformity achieved here motivate the development of a uniform breakage process, described in the next subsection.

3.3. Design Noncontact Sonication in Slug Flow for Uniform Crystal Breakage

The goal is to reduce crystal dimensions—length, width, and aspect ratio—while maintaining uniformity across the population. Uniform crystal breakage is achieved by applying sonication to uniform-size flowing slurry slugs, for a similar reason for spatial uniformity as described in the previous subsection. Sonication may be introduced through either a sonication bath or a noncontact probe. From preliminary observations (Figure 8a), the width of needle-shaped crystals changes very little during sonication, whereas the length decreases by more than 80% within 10 min. Because the

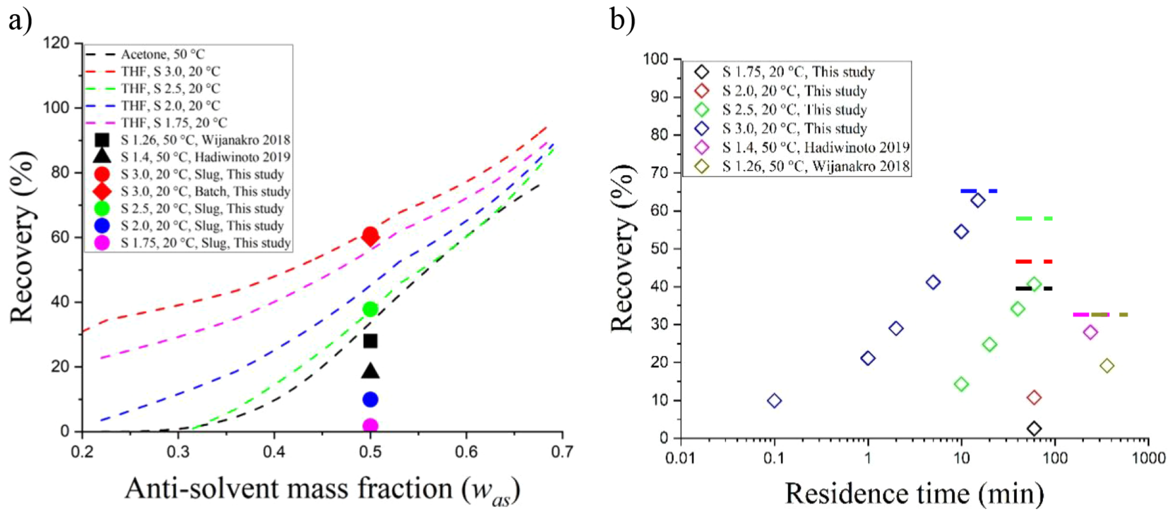

Figure 7. (a) Actual RPT recovery at different antisolvent mass fractions (w_{AS}) or supersaturations (S_i = 1.75−3.0), compared to literature values and theoretical recovery (dashed lines). (b) Actual and theoretical recovery at different residence times, using the same symbols as (a).

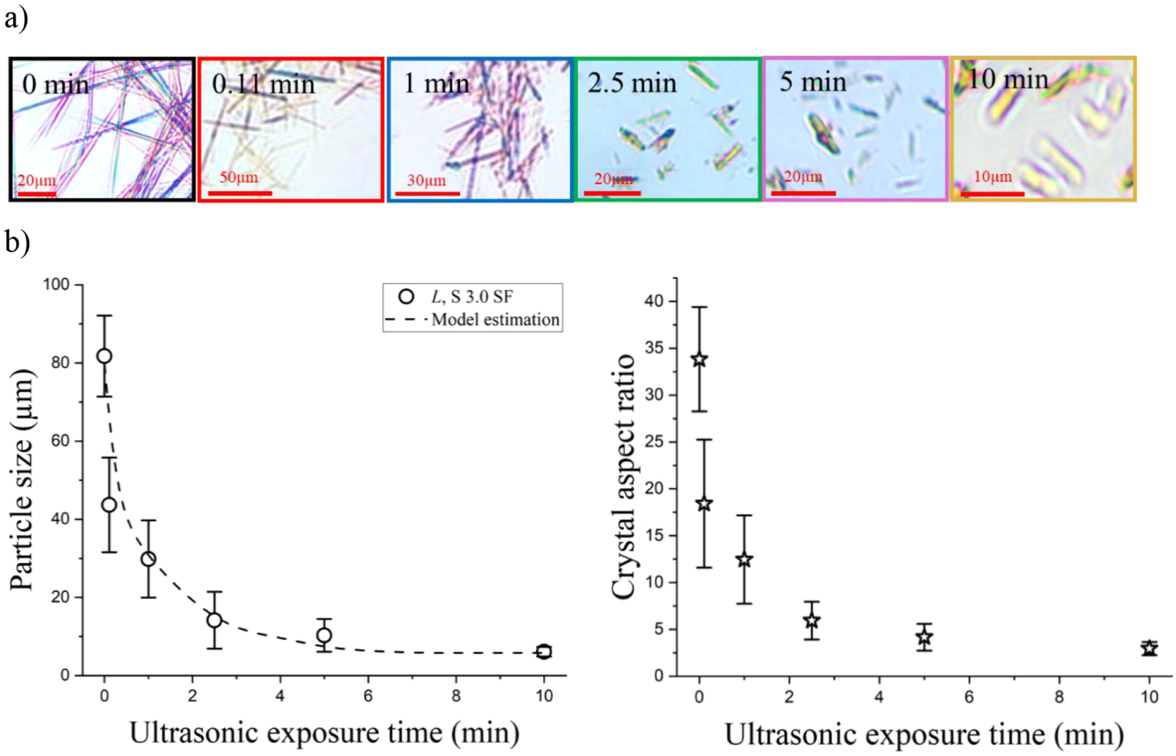

Figure 8. (a) Representative microscope images of RPT crystals in slug flow under sonication, at varying exposure times. (b) Crystal length and aspect ratio for (a), from model predictions (dashed line) and experiment validations.

crystals remain significantly longer than they are wide, the assignment of “length” and “width” for each crystal remains the same throughout the process. Thus, we treat length reduction as independent of width and assume that total crystal length is conserved during breakage. The model is therefore formulated for length only. Following the scaling analysis detailed in Appendix A2, the number-average crystal length within a representative slug can be approximated using a population-level breakage model based on two assumptions: (i) sonofragmentation produces binary fragments within the range 0.3−0.7, and (ii) the breakage probability is proportional to the square root of crystal length (statistical interpretation of Griffith’s scaling).[53−55]

Under these assumptions, the number-average length obeys the differential equation $\mathrm{d}L/\mathrm{d}t = -aL^{3/2}$, and its analytical solution: $L(t) = 1/[(a/2)t + L_0^{-1/2}]^2$, where L_0 is the initial number-average length, and a is one lumped parameter capturing effects of surface tension, sonication intensity, defect crystal density, and fracture strength.[53−55] This expression reflects the same scaling behavior as the characteristic size in a self-similar breakage population, where the number-average length follows the same time dependence as the single-crystal breakage law. The analytical form of $L(t)$ indicates that length decreases more rapidly than width, because the breakage rate scales with $L^{3/2}$. The model also predicts a practical “stabilized” length: once the residence time becomes large enough that doubling it changes $L(t)$ by less than ~10%, further sonication yields diminishing returns. This plateau is not a true physical asymptote but an engineering threshold arising from the t^{-2} decay.

Because parameters such as defect density and local acoustic intensity are difficult to measure directly, the value of parameter a (e.g., 0.135 $\mu m^{-1/2}$ min^{-1}) is estimated from small-scale calibration experiments using a few slugs at several time points (e.g., 0, 1, and 2.5 min) using the same platform. Based on uniformity in slug flow, the fitted value of a is assumed constant over the relevant residence-time range for each slug. Once calibrated, the model can be used to predict crystal length and width at other sonication times. This "scaling down" flow design was supported by earlier demonstration with scalable reaction crystallization in slug flow,[48] by running the same process (e.g., reactant flow rates, solution concentration) for different time while maintaining each slug the same (variation of <0.02 among slugs). Here we replace two reactant streams with solvent and antisolvent streams.

Sonicating slurry slugs enables rapid and reproducible reduction of crystal length and aspect ratio to target ranges (e.g., from 81 to 6 μm in length; aspect ratio from 33 to 3.5), while maintaining 100% Form I (Figure S4). The final values obtained in a 60 mL slug-flow system (Figure 8b) closely match both small-slug experiments (<0.2 mL) and model predictions. The dynamic trends also agree with the model: length decreases much faster than width, and it approaches a practical stabilized value beyond which additional sonication produces minimal change. With negligible changes in crystal width over the residence times tested, the aspect ratio exhibits decay dynamics similar to those of crystal length. Deviations at intermediate or extrapolated times may arise from changes in the effective parameter a_s, such as evolving defect density or increasing crystal number density. With the narrow residence-time distribution characteristic of slug flow,[48,56−58] crystal dimensions converge rapidly (within ~10 min) to their stabilized values with small variation (e.g., $CV_L \sim 0.20$, $CV_W \sim 0.17$, $CV_{AR} \sim 0.29$). In contrast, batch sonofragmentation requires roughly twice the time (~20 min) to reach similar sizes. This improvement likely arises from more uniform acoustic exposure and more efficient energy delivery within each slug compared to a stirred tank.

4. CONCLUSIONS

We developed a scalable, nonfouling continuous antisolvent crystallization process by integrating precise antisolvent injection, fouling-free supersaturation control, and strategically timed noncontact sonication within a tubular slug-flow platform. To achieve subsecond, reproducible antisolvent dosing into individual slugs, we generated discrete antisolvent droplets that merge with solution slugs at precise intervals—eliminating the need for faster feedback control. We established design criteria that ensure uniformity and reproducibility: (1) maintaining hydrodynamic slug stability before and after injection by tuning the total liquid-to-gas flow-rate ratio, enabling consistent formation of short solution slugs ($0.4 < L_{L,sol}/d < 0.5$) that expand into longer mixture slugs ($0.8 < L_{L,mix}/d < 1.0$); (2) ensuring reproducible droplet growth and stability via inertial scaling of droplet height, $H(t) = A_h \cdot t^{1/2}$, such as timing just before $H(t)$ reached the tube *I.D.*; and (3) synchronizing droplet predetachment formation with slug arrival by adjusting slug spacing and velocity to satisfy $\tau_{fall}/\tau_{slug} > 1$. This design achieves highly consistent antisolvent injection with minimal volume variation ($CV = 0.014$), enabling reproducible nucleation, growth, and breakage, demonstrated here using rifapentine.

To achieve uniform nucleation and growth without fouling, we codesigned flow conditions, supersaturation control, and noncontact sonication. The inherent uniformity within and between slugs was leveraged to generate spatially uniform acoustic "milli-fields." For nucleation, sonication applied immediately after antisolvent injection—where supersaturation peaks and fouling risk is highest—reduced mixing time far more than induction time (e.g., a 10-fold greater reduction at $S_i = 2.0$), achieving $\tau_{mix} \ll \tau_{ind}$ and eliminating local supersaturation hotspots. Experiments validated model predictions that $S_i \leq 3.0$ prevents fouling and yields uniform nuclei ($L \approx 3$ μm, $CV \approx 0.1$). For growth, a second sonication step dispersed early agglomerates and maintained narrow size distributions even as crystals grew to 81 μm in length with an aspect ratio of 33. This codesigned strategy reduced crystallization residence time from 4−6 to 0.25 h while approaching the theoretical 63% recovery for an antisolvent mass fraction of 0.5. Future work may further increase recovery and reduce aspect ratio while preserving crystal uniformity.

For uniform crystal breakage, we applied noncontact sonication to flowing slurry slugs. Preliminary results show that sonication reduces crystal length by more than 80% within 10 min while leaving width nearly unchanged, enabling a simplified length-only breakage model. Assuming binary fragmentation and $L^{1/2}$ scaling of breakage probability, the number-average length follows $L(t) = 1/[(a/2)t + L_0^{-1/2}]^2$, indicating a t^{-2} decay and an engineering "stabilized" final size within practical operating times. Owing to the uniformity and reproducibility of the codesigned system, a small-scale (0.16 mL) calibration experiment at selected times was sufficient to determine a and accurately predict breakage outcomes (length, width) and required processing times for both other time points and a larger 60 mL volume. In practice, slug-flow sonication rapidly produces uniform, shortened crystals (e.g., 81 μm → 6 μm; aspect ratio 33 → 3.5; $CV_L \sim 0.20$, $CV_W \sim 0.17$, $CV_{AR} \sim 0.29$; 100% Form I) with narrower size distributions and faster convergence than batch sonication.

ASSOCIATED CONTENT

Supporting Information

The Supporting Information is available free of charge at https://pubs.acs.org/doi/10.1021/acs.cgd.5c01079.

Characterization (DSC, TGA, XRD, and microscope image) of starting and recrystallized RPT, statistical analysis of crystal length, width, and aspect ratio (PDF)

AUTHOR INFORMATION

Corresponding Author

Mo Jiang − *Department of Chemical and Life Science Engineering, Virginia Commonwealth University, Richmond, Virginia 23284, United States; The Polytechnic School, Arizona State University, Mesa, Arizona 85212, United States;* orcid.org/0000-0002-6620-2997;
Email: mojiang@asu.edu

Authors

Sunuk Kim − *Department of Chemical and Life Science Engineering, Virginia Commonwealth University, Richmond,* *Virginia 23284, United States; The Polytechnic School, Arizona State University, Mesa, Arizona 85212, United States*

Huayu Li − *Material and Analytical Sciences, Boehringer Ingelheim Pharmaceuticals Inc., Ridgefield, Connecticut 06877, United States;* orcid.org/0000-0003-1292-297X

Richard D. Braatz − *Department of Chemical Engineering, Massachusetts Institute of Technology, Cambridge, Massachusetts 02139, United States;* orcid.org/0000-0003-4304-3484

Tai-Yuen Yue − *Department of Chemical and Life Science Engineering, Virginia Commonwealth University, Richmond, Virginia 23284, United States;* orcid.org/0000-0002-9131-2709

B. Frank Gupton − *Department of Chemical and Life Science Engineering, Virginia Commonwealth University, Richmond, Virginia 23284, United States;* orcid.org/0000-0002-8165-1088

Bing-Shiou Yang − *Material and Analytical Sciences, Boehringer Ingelheim Pharmaceuticals Inc., Ridgefield, Connecticut 06877, United States*

Complete contact information is available at:
https://pubs.acs.org/10.1021/acs.cgd.5c01079

Notes

The authors declare no competing financial interest.

ACKNOWLEDGMENTS

Kwame Markin and Carter Miller are acknowledged for discussion and manuscript proofreading.

ABBREVIATIONS

AR	Crystal aspect ratio (L/W), dimensionless
a_s	A lumped breakage parameter, $\mu m^{-1/2} \cdot min^{-1}$
Bo	Bond number ($0394 \rho g D^2/\gamma$), dimensionless
Bo_{max}	Max Bond number, dimensionless
C	Solute concentration, kg/m^3
$C*$	Saturated solute concentration, kg/m^3
C_c	Calibration constant for matching deposition rate unit, 0.413 $kg^{0.5}/m^{0.1} \cdot s^{2.4} \cdot K^{0.5}$
C_s	Solubility, mg/mL or kg/m^3
CV	Coefficient variation, dimensionless
CV_{AR}	Coefficient variation of particle aspect ratio, dimensionless
CV_L	Coefficient variation of particle length, dimensionless
CV_V	Coefficient variation of liquid slug volume change, dimensionless
CV_W	Coefficient variation of particle width, dimensionless
d	tube inner diameter of main reactor, mm
G	Growth rate, $\mu m/min$
H	Antisolvent droplet diameter (height), mm
H_{crit}	Critical droplet diameter (height) for detachment of droplet on inlet, m
J	Nucleation rate, $ml^{-1} \cdot s^{-1}$
I	Postoperation transmitted light intensity, a.u.
I_0	Preoperation transmitted light intensity, a.u.
L	RPT particle length, μm
L_G	Gas slug length, mm
$L_{L,sol}$	Preinjection liquid slug length, mm
$L_{L,mix}$	Postinjection liquid slug length, mm
L_0	Initial length of RPT particle, μm
N_v	Particles number density, Particles/mL
Q_G	Volumetric flow rate of gas, mL/min
Q_L	Volumetric flow rate of liquid, mL/min
$Q_{L,inj}$	Volumetric flow rate of antisolvent, mL/min
$Q_{L,sol}$	Volumetric flow rate of solution, mL/min
$Q_{L,T}$	Volumetric flow rate of total liquid (sol+anti), mL/min
S	Relative supersaturation ($C/C*$), dimensionless
t_s	ultrasonic exposure time, min
U_G	Superficial velocities of gas, m/s
U_L	Superficial velocities of liquid, m/s
$U_{L,inj}$	Superficial velocities of antisolvent, m/s
$U_{L,sol}$	Superficial velocities of RPT solution, m/s
V_s	Liquid slug volume, μL
v_s	Superficial velocity of slug flow, m/s
W	RPT particle width, μm
w_{AS}	Antisolvent mass fraction, dimensionless
ε	Liquid and gas flow rate ratio, dimensionless
τ_{fall}	The time of droplet falling out, s
τ_{ind}	Induction time, s
τ_{mix}	Slug macro-mixing time, s
τ_{slug}	Slug residence time or time interval between adjacent slugs, s
τ_{res}	Crystallization residence time, min or h
φ	Ratio of solvent to antisolvent mass flow, dimensionless

REFERENCES

(1) Dickinson, J. M.; Mitchison, D. A. In Vitro Properties of Rifapentine (MDL473) Relevant to Its Use in Intermittent Chemotherapy of Tuberculosis. *Tubercle* **1987**, *68* (2), 113−118.

(2) Fund, G.; Aids, F.; Sa, S.; Partnership, S. T. B.; Sa, S.; Fund, G.; Sa, S.; Sa, S.; Partnership, S. T. B.; Facility, G. D. *Rifapentine Global Price Discount*; Global Drug Facility, 2018.

(3) Treatment Action Group *An Activist's Guide To Rifapentine For The Treatment Of TB Infection*, 2020. https://www.treatmentactiongroup.org/wp-content/uploads/2020/04/rifapentine_guide_2020.pdf.

(4) Treatment Action Group *An Activist's Guide To Rifapentine For The Treatment Of TB*, 2024. https://www.treatmentactiongroup.org/wp-content/uploads/2024/05/rifapentine_guide_2024_final.pdf.

(5) Wijanarko, A.; Meivita, M. P.; Hermansyah, H.; Sahlan, M.; Lakerveld, R. Batch Crystallization of Rifapentine for Inhalable Tuberculosis Medication. *AIP Conf. Proc.* **2018**, *1933*, 030023.

(6) Hadiwinoto, G. D.; Kwok, P. C. L. L.; Tong, H. H. Y. Y.; Wong, S. N.; Chow, S. F.; Lakerveld, R. Integrated Continuous Plug-Flow Crystallization and Spray Drying of Pharmaceuticals for Dry Powder Inhalation. *Ind. Eng. Chem. Res.* **2019**, *58* (36), 16843−16857.

(7) Civati, F.; O'Malley, C.; Erxleben, A.; McArdle, P. Factors Controlling Persistent Needle Crystal Growth: The Importance of Dominant One-Dimensional Secondary Bonding, Stacked Structures, and van Der Waals Contact. *Cryst. Growth Des.* **2021**, *21* (6), 3449−3460.

(8) Pu, S.; Hadinoto, K. Habit Modification in Pharmaceutical Crystallization: A Review. *Chem. Eng. Res. Des.* **2024**, *201* (July 2023), 45−66.

(9) Horio, T.; Yasuda, M.; Matsusaka, S. Effect of Particle Shape on Powder Flowability of Microcrystalline Cellulose as Determined Using the Vibration Shear Tube Method. *Int. J. Pharm.* **2014**, *473* (1−2), 572−578.

(10) Ho, R.; Naderi, M.; Heng, J. Y. Y.; Williams, D. R.; Thielmann, F.; Bouza, P.; Keith, A. R.; Thiele, G.; Burnett, D. J. Effect of Milling on Particle Shape and Surface Energy Heterogeneity of Needle-Shaped Crystals. *Pharm. Res.* **2012**, *29* (10), 2806−2816.

(11) Širola, I.; Lukšić, J.; Šimunić, B.; Kujundžić, N. Effect of Crystal Size and Shape on Bulk Density of Pharmaceutical Powders. *J. Cryst. Growth* **1997**, *181* (4), 403−409.

(12) Mahdi, F. M.; Shier, A. P.; Fragkopoulos, I. S.; Carr, J.; Gajjar, P.; Muller, F. L. On the Breakage of High Aspect Ratio Crystals in

Filter Beds under Continuous Percolation. *Pharm. Res.* **2020**, *37* (12), 231.

(13) Zhou, K.; Li, J.; Luo, J.; Zheng, D. Crystal Modification of Rifapentine Using Different Solvents. *Front. Chem. Eng. China* **2010**, *4* (1), 65−69.

(14) Nebuloni, M.; Occelli, E.; Cavalleri, B. Pure Crystalline Form of Rifapentine WO 1,992,000,302 A1, 1991.

(15) Chan, J. G. Y.; Duke, C. C.; Ong, H. X.; Chan, J. C. Y.; Tyne, A. S.; Chan, H. K.; Britton, W. J.; Young, P. M.; Traini, D. A Novel Inhalable Form of Rifapentine. *J. Pharm. Sci.* **2014**, *103* (5), 1411−1421.

(16) Zhou, K.; Li, J.; Luo, J.; Jin, Y. Crystal Growth, Structure and Morphology of Rifapentine Methanol Solvate. *Chin. J. Chem. Eng.* **2012**, *20* (3), 602−607.

(17) Lin, X.; Li, J.; Hu, J. The Preparation Method of Rifapentine CN 103,951,677 B, 2014.

(18) Gu, Y.; Xu, K.; Yan, W.; Liu, R.; Wang, Y. Preparation Method of High-Purity Rifapentine CN 103,951,677 B, 2020.

(19) Yuan, S.; Duan, C.; Liu, Y.; Yang, L.; Chen, H. Mechanistic Insights into the Link between Milling-Induced Surface Layer Particle Damage and Mechanical Property Evolution of SiCp/2009Al Composite Thin-Walled Parts. *J. Mater. Process. Technol.* **2025**, *342* (May), 118932.

(20) Li, P.; Chen, C.; Zhang, C.; Xiao, N.; Zhang, H.; Li, Y.; Guo, Z. Effects of Ball Milling on Powder Particle Boundaries and Properties of ODS Copper. *High Temp. Mater. Process* **2021**, *40* (1), 361−369.

(21) Agimelen, O. S.; Svoboda, V.; Ahmed, B.; Cardona, J.; Dziewierz, J.; Brown, C. J.; McGlone, T.; Cleary, A.; Tachtatzis, C.; Michie, C.; et al. Monitoring Crystal Breakage In Wet Milling Processes Using Inline Imaging And Chord Length Distribution Measurements, **2017**, DOI: .

(22) Gao, Y.; Song, W.; Yang, J.; Ji, X.; Wang, N.; Huang, X.; Wang, T.; Hao, H. Crystal Morphology Prediction Models and Regulating Methods. *Crystals* **2024**, *14* (6), 484.

(23) Parker, A. S. *Solid State Crystallization of Amorphous Pharmaceuticals in an Aqueous Environment: factors Impacting Crystallization and the Role of Additives*; Purdue University, 2021.

(24) Hadjittofis, E.; Isbell, M. A.; Karde, V.; Varghese, S.; Ghoroi, C.; Heng, J. Y. Y. Influences of Crystal Anisotropy in Pharmaceutical Process Development. *Pharm. Res.* **2018**, *35* (5), 100.

(25) Jikazana, A.; Garg, K.; Le Corre Pidou, K.; Campo, P.; McAdam, E. J. The Role of Mixing on the Kinetics of Nucleation and Crystal Growth in Membrane Distillation Crystallisation. *Sep. Purif. Technol.* **2025**, *353* (PC), 128533.

(26) Jordens, J.; Appermont, T.; Gielen, B.; Van Gerven, T.; Braeken, L. Sonofragmentation: Effect of Ultrasound Frequency and Power on Particle Breakage. *Cryst. Growth Des.* **2016**, *16* (11), 6167−6177.

(27) Bałdyga, J. Mixing and Fluid Dynamics Effects in Particle Precipitation Processes. *KONA Powder Part. J.* **2016**, *33*, 127−149.

(28) Koswara, A.; Nagy, Z. K. Anti-Fouling Control of Plug-Flow Crystallization via Heating and Cooling Cycle. *IFAC-Papersonline* **2015**, *28* (8), 193−198.

(29) Madane, K.; Ranade, V. V. Anti-Solvent Crystallization: Particle Size Distribution with Different Devices. *Chem. Eng. J.* **2022**, *446* (P3), 137235.

(30) Miller, R.; Sefcik, J.; Lue, L. Modeling Diffusive Mixing in Antisolvent Crystallization. *Cryst. Growth Des.* **2022**, *22* (4), 2192−2207.

(31) Schlüter, F.; Schnöing, L.; Zettler, H.; Augustin, W.; Scholl, S. Measuring Local Crystallization Fouling in a Double-Pipe Heat Exchanger. *Heat Transfer. Eng.* **2020**, *41* (2), 149−159.

(32) Sauret, A.; Somszor, K.; Villermaux, E.; Dressaire, E. Growth of Clogs in Parallel Microchannels. *Phys. Rev. Fluids* **2018**, 3 (10), 1−18.

(33) Berce, J.; Zupančič, M.; Može, M.; Golobič, I. A Review of Crystallization Fouling in Heat Exchangers. *Processes* **2021**, *9* (8), 1356.

(34) O'Donoghue, L. T.; Haque, M. K.; Kennedy, D.; Laffir, F. R.; Hogan, S. A.; O'Mahony, J. A.; Murphy, E. G. Influence of Particle Size on the Physicochemical Properties and Stickiness of Dairy Powders. *Int. Dairy J.* **2019**, *98*, 54−63.

(35) Zhao, X.; Chen, X. D. A Critical Review of Basic Crystallography to Salt Crystallization Fouling in Heat Exchangers. *Heat Transfer Eng.* **2013**, *34* (8−9), 719−732.

(36) Aghapour Aktij, S.; Taghipour, A.; Rahimpour, A.; Mollahosseini, A.; Tiraferri, A. A Critical Review on Ultrasonic-Assisted Fouling Control and Cleaning of Fouled Membranes. *Ultrasonics* **2020**, *108* (July), 106228.

(37) Zhou, Q.; Sun, S. P.; Chan, J. G. Y.; Wang, P.; Barraud, N.; Rice, S. A.; Wang, J.; Li, J.; Chan, H. K. Novel Inhaled Combination Powder Containing Amorphous Colistin and Crystalline Rifapentine with Enhanced Antimicrobial Activities against Planktonic Cells and Biofilm of Pseudomonas Aeruginosa for Respiratory Infections. *Mol. Pharmaceutics* **2015**, *12* (8), 2594−2603.

(38) Ecolink Inc *Tetrahydrofuran (THF) 55-Gallon Drum Commodity Grade*; Ecolink Inc.: Tucker, GA, USA. https://ecolink.com/shop/commodities/tetrahydrofuran-thf-55-gallon-drum/.

(39) Ecolink Inc ACETONE − 55 Gallon Drum; Ecolink Inc: Tucker, GA, USA.

(40) Jiang, M.; Papageorgiou, C. D.; Waetzig, J.; Hardy, A.; Langston, M.; Braatz, R. D. Indirect Ultrasonication in Continuous Slug-Flow Crystallization. *Cryst. Growth Des.* **2015**, *15* (5), 2486−2492.

(41) Jiang, M.; Gu, C.; Braatz, R. D. Analysis of Focused Indirect Ultrasound via High-Speed Spatially Localized Pressure Sensing and Its Consequences on Nucleation. *Chem. Eng. Process. Process Intensif.* **2017**, *117* (January), 186−194.

(42) Triplett, K. A.; Ghiaasiaan, S. M.; Abdel-Khalik, S. I.; Sadowski, D. L. Gas-Liquid Two-Phase Flow in Microchannels Part I: Two-Phase Flow Patterns. *Int. J. Multiph. Flow* **1999**, *25* (3), 377−394.

(43) Ghajar, A. J. Non-Boiling Heat Transfer in Gas-Liquid Flow in Pipes - A Tutorial. *J. Brazilian Soc. Mech. Sci. Eng.* **2005**, *27* (1), 46−73.

(44) Mou, M.; Jiang, M. Fast Continuous Non-Seeded Cooling Crystallization of Glycine in Slug Flow: Pure α-Form Crystals with Narrow Size Distribution. *J. Pharm. Innov.* **2020**, *15* (2), 281−294.

(45) Burton, J. C.; Waldrep, R.; Taborek, P. Scaling and Instabilities in Bubble Pinch-Off. *Phys. Rev. Lett.* **2005**, *94* (18), 1−4.

(46) Fries, D. M.; von Rohr, P. R. Impact of Inlet Design on Mass Transfer in Gas-Liquid Rectangular Microchannels. *Microfluid. Nanofluidics* **2009**, *6* (1), 27−35.

(47) Mou, M.; Dela Rosa, L.; Mugumya, J. H.; Jiang, M. Continuous Generation of Gas-Water Slugs with Improved Size Uniformity at a Tunable Scale. *Chem. Eng. Technol.* **2023**, *46* (10), 2073−2080.

(48) Kim, S.; Jiang, M. Direct Precipitation Pathway to Pure α-MnC2O4·2H2O Using Slug Flow toward the Scalable Nonfouling Fast Synthesis of Uniform Microcrystals. *Cryst. Growth Des.* **2024**, *24*, 2672.

(49) Jiang, H.; Wang, J.; Li, J.; Sun, N. Study on Deposition Rate Model Optimization of Crystallization Fouling. *J. Eng. Thermophys.* **2023**, *32* (1), 162−179.

(50) Pääkkönen, T. M.; Riihimäki, M.; Simonson, C. J.; Muurinen, E.; Keiski, R. L. Crystallization Fouling of CaCO3 - Analysis of Experimental Thermal Resistance and Its Uncertainty. *Int. J. Heat Mass Transfer.* **2012**, *55* (23−24), 6927−6937.

(51) Hashmi, A.; Xu, J. On the Quantification of Mixing in Microfluidics. *J. Lab. Autom.* **2014**, *19* (5), 488−491.

(52) Vamsi Krishna, M.; Ramesh Babu, J.; Latha, P. V. M.; Gowri Sankar, D. Sonocrystallization: For Better Pharmaceutical Crystals. *Asian J. Chem.* **2007**, *19* (2), 1369−1374.

(53) Suslick, S. Sonochemistry. *Science* **1990**, *247* (4949), 1439−1445.

(54) Chen, J. H.; Cao, R. Introduction. In *Micromechanism of Cleavage Fracture of Metals*; Elsevier, 2015; pp. 1−54. DOI: .

(55) Rasche, M. L.; Zeiger, B. W.; Suslick, K. S.; Braatz, R. D. Mathematical Modelling of the Evolution of the Particle Size Distribution during Ultrasound-Induced Breakage of Aspirin Crystals. *Chem. Eng. Res. Des.* **2018**, *132*, 170−177.

(56) Jiang, M.; Zhu, Z.; Jimenez, E.; Papageorgiou, C. D.; Waetzig, J.; Hardy, A.; Langston, M.; Braatz, R. D. Continuous-Flow Tubular Crystallization in Slugs Spontaneously Induced by Hydrodynamics. *Cryst. Growth Des.* **2014**, *14* (2), 851−860.

(57) Jiang, M.; Braatz, R. D. Designs of Continuous-Flow Pharmaceutical Crystallizers: Developments and Practice. *CrystEngcomm* **2019**, *21* (23), 3534−3551.

(58) Moschou, P. *Evaporation and Crystallization in Micro Flow Systems*; Eindhoven University of Technology, 2014, Vol. *1*. DOI: .